Available online at www.sciencedirect.com
SCIENCE DIRECT
Earth and Planetary Science Letters 245 (2006) 730–742
EPSL
www.elsevier.com/locate/epsl

Carbon solubility in mantle minerals

Svyatoslav S. Shcheka [a,b,*], Michael Wiedenbeck [c], Daniel J. Frost [b], Hans Keppler [a,b]

[a] Institut für Geowissenschaften, Universität Tübingen, Wilhelmstr. 56, 72074 Tübingen, Germany
[b] Bayerisches Geoinstitut, Universität Bayreuth, 95440 Bayreuth, Germany
[c] GeoForschungsZentrum Potsdam, Telegrafenberg, 14473 Potsdam, Germany

Received 21 October 2005; received in revised form 20 March 2006; accepted 23 March 2006
Available online 2 May 2006
Editor: G.D. Price

Abstract

The solubility of carbon in olivine, enstatite, diopside, pyrope, $MgAl_2O_4$ spinel, wadsleyite, ringwoodite, $MgSiO_3$–ilmenite and $MgSiO_3$–perovskite has been quantified. Carbon-saturated crystals were grown from carbonatite melts at 900–1400 °C and 1.5 to ~ 26 GPa in piston cylinder or multi-anvil presses using carbon enriched to >99% in the ^{13}C isotope. In upper mantle silicates, carbon solubility increases as a function of pressure to a maximum of ~ 12 ppm by weight in olivine at 11 GPa. No clear dependence of carbon solubility on temperature, oxygen fugacity or iron content was observed. The observation that carbon solubility in olivine is insensitive to oxygen fugacity implies that the oxidation state of carbon in the carbonatite melt and in olivine is the same, i.e., carbon dissolves as C^{4+} in olivine. Carbon solubility in spinel $MgAl_2O_4$, transition zone minerals (wadsleyite and ringwoodite), $MgSiO_3$–ilmenite and $MgSiO_3$–perovskite are below the limit of detection of our SIMS-based analytical technique (i.e., below 30–200 ppb by weight). The differences in carbon solubilities between the various minerals studied appear to correlate with the polyhedral volume of the Si^{4+} site, consistent with a direct substitution of C^{4+} for Si^{4+}. These results show that other, minor carbon-rich phases, rather than major, nominally volatile-free minerals, dominate the carbon budget within the bulk Earth's mantle. A significant fraction of total carbon could only be stored in silicates in a thin zone in the lowermost upper mantle, just above the transition zone, and only if the bulk carbon content is at the lower limit of published estimates. The carbon budget of the remaining mantle is dominated by carbonates and possibly diamond. The low melting point of carbonates and the high mobility of carbonate melts suggest that carbon distribution in the mantle may be highly heterogeneous, including the possibility of massive carbon enrichments on a local scale, particularly in the shallow subcontinental mantle.

Keywords: carbon; carbon dioxide; carbonates; mantle; high pressure; SIMS

1. Introduction

Only a small fraction of the total carbon budget of our planet is located in near-surface reservoirs [1,2]. Although some carbon might be stored in the core [3,4], the mantle is thought to be the Earth's largest carbon reservoir [5].

Carbon may be stored in the mantle as carbonates, graphite, diamond or as C–H–O fluids [6]. Carbon-bearing fluids in the mantle are usually dominated by CO_2, but under very reducing conditions, CH_4 may also become important. Alternatively, traces of carbon may be dissolved in common, nominally volatile-free silicates. A significant solubility of carbon in mantle silicates is suggested by fluid inclusions. Brewster in 1823 [7] first

* Corresponding author. Bayerisches Geoinstitut, Universität Bayreuth, 95440 Bayreuth, Germany. Tel.: +49 921 553745; fax: +49 921 553769.
E-mail address: Svyatoslav.Shcheka@uni-bayreuth.de (S.S. Shcheka).

0012-821X © 2006 Elsevier B.V. Open access under CC BY-NC-ND license.
doi:10.1016/j.epsl.2006.03.036

observed the ubiquitous presence of tiny (<1 μm) bubbles in minerals from peridotite xenoliths in alkali basalts. The bubbles were filled with "a mysterious fluid with remarkable physical properties," later identified as nearly pure liquid carbon dioxide [8,9]. These observations were interpreted as evidence that such C-rich inclusions formed by the exsolution of carbon dioxide [10,11], originally dissolved in host minerals at higher pressure. Alternatively, they may represent fluid trapped during crystal growth from a melt or during subsequent healing of fractures in crystals [12,13]. Four observations support the former interpretation: (1) The bubbles are extremely small; (2) they are located on dislocations or other defects in the crystal structure; (3) they are concentrated on the boundaries of inclusion-free recrystallized grains [10]; and (4) the bubbles appear to dissolve into the host olivine at pressures up to 110 kbar during annealing experiments [14].

Green and Guegen [11] estimated that the volume fraction of carbon dioxide inclusions in olivine from a peridotite xenolith in a kimberlite corresponds to a carbon solubility of 160 ppm by weight (ppmw), assuming a positive pressure dependence of solubility. Comparing this number with estimates of bulk carbon abundance of upper mantle (from 53 to 72 ppmw in depleted MORB source to >1000 ppmw in more primitive mantle [5,15,16]) would suggest that there might be regions in the upper mantle where a significant fraction, if not all of the carbon, could be accommodated by normally volatile-free silicates.

Numerous attempts to determine carbon solubility in olivine since the early 1980s [17–21] have yielded contradicting results, probably reflecting sample contamination problems. Recent data by Keppler et al. [22] suggest that normal upper mantle silicates may dissolve only traces of carbon (1–5 ppm by weight). However, a systematic study of carbon solubility in the nominally volatile-free minerals stable throughout the entire mantle remains lacking. In particular, little is known about the behavior of carbon in the transition zone and lower mantle. There are no data on carbon solubility in wadsleyite, ringwoodite, $MgSiO_3$–ilmenite and the major phase of the lower mantle, $MgSiO_3$–perovskite. Carbonates, particularly magnesite and its high-pressure polymorphs, are stable throughout most of the mantle [23–25], with diamond becoming stable in more reduced regions [26,27]. However, as $MgSiO_3$–perovskite is the most abundant mineral on Earth, even a moderate solubility of carbon would make $MgSiO_3$–perovskite in the lower mantle the largest carbon reservoir on our planet.

Here we report carbon solubility in olivine at various pressures, temperatures and redox conditions, the first precise measurements of carbon solubility in $MgAl_2O_4$ spinel, enstatite, diopside and pyrope and the first data on carbon solubility in wadsleyite, ringwoodite, $MgSiO_3$–ilmenite and $MgSiO_3$–perovskite. These data therefore cover the entire range of nominally volatile-free minerals of the Earth's mantle.

2. Experimental technique

Stoichiometric mixtures for each mineral of interest were prepared from high-purity oxides and hydroxides and were ground together with 10–20 wt.% of Na_2CO_3 certified to contain more than 99% of the ^{13}C isotope. For piston cylinder experiments, these mixtures together with about 1% of water were loaded in 10-mm-long capsules with an outer diameter of 5 mm and a wall thickness of 0.3 mm made of platinum–rhodium (95 wt.% Pt, 5 wt.% Rh), iron, cobalt or nickel. Platinum–rhodium capsules were sealed by arc welding. Iron, cobalt and nickel capsules were mechanically sealed by forcing a tightly fitting lid into the capsule. In multi-anvil runs, we used platinum capsules (1–3.5 mm long, 1–2 mm in diameter) made from 0.1-mm-thick foil.

Experiments at 1.5 GPa pressure and 900–1100 °C were carried out in a non-end-loaded Johannes-type [28] piston cylinder (PC) apparatus. Assemblies (22 mm diameter, 45 mm long) consisted of NaCl, Pyrex glass, crushable alumina, pyrophyllite and graphite. A tapered graphite heater was used to minimize thermal gradient [29]. Temperatures were measured by a NiCr–Ni (K type) thermocouple which physically contacted the sample capsule. Pressures reported include a 10% friction correction. Pressures and temperatures are estimated to be accurate to ±0.1 GPa and ±25 °C. Oxygen fugacity was not strictly controlled in runs with PtRh capsules, but the reaction of traces of water with the graphite heater results in an oxygen fugacity close to Ni–NiO buffer. The oxidation of the Fe, Co and Ni capsules in experiments Ol-11F1, Ol-11C and Ol-11N produced oxygen fugacities corresponding to the Fe–FeO (iron–wüstite), Co–CoO, and Ni–NiO buffers, respectively.

Experiments performed at 6–26 GPa and 900–1400 °C employed 500- and 1000-tonne multi-anvil presses using 32-mm Toshiba tungsten carbide cubes, pyrophyllite gaskets and 18/11 (octahedral edge length/truncation edge length), 14/8, 10/5, 10/4, and 8/3 octahedral sample assemblies made from partially sintered, Cr-doped MgO (95% MgO+5% Cr_2O_3). A $LaCrO_3$ heater (with stepped design in the 18/11 and 14/8 assemblies to reduce temperature gradients [30]) was separated from the octahedron by a ZrO_2 sleeve and from the capsule by a MgO sleeve. The capsule was positioned near the middle of the assembly by crushable alumina or MgO spacers. A W3Re97–W25Re75 thermocouple was

inserted axially in a four-bore Al_2O_3 ceramic rod with the hot junction next to a Re-foil disc placed between thermocouple and capsule. No correction for the effect of pressure on the emf of the thermocouple was applied. Pressure calibrations have been published elsewhere ([31,32] and references therein) and are estimated to have an accuracy of ±5%. As in most piston-cylinder experiments, the redox state was not controlled, but the presence of amorphous carbonaceous material coexisting with carbonates in several multi-anvil runs shows that equilibria similar to $MgSiO_3+MgCO_3=Mg_2SiO_4+C+O_2$ [33,34] probably yield an oxygen fugacity between the EMOG(D) and GCO buffers [34–36].

In all experiments, assemblies were firstly compressed to the final pressure and then temperature was increased at a rate of 50–100 °C/min. All runs were quenched to room temperature within a few seconds by switching off the power to the heater.

Recovered capsules were punctured, dried at 150 °C for 1 h and weighed before and after drying. A loss of weight due to the release of water indicated that the capsule remained sealed throughout the experiment. Another sign of the impermeability of the capsule during the run was the evolution of carbon dioxide when nitric acid was added to the run products. Those experiments which did not show both features were discarded.

Because the aim of the experiments was to produce crystals saturated with the ^{13}C isotope and because diffusion of carbon from the graphite heater into the Pt capsule might be significant in piston cylinder runs (see [37] for review), infrared spectra of carbonates recovered after test experiments were compared to that of the $Na_2^{13}CO_3$ used in starting mixtures and to Na_2CO_3 with natural isotopic composition. Fig. 1 demonstrates that only minor amounts of ^{12}C are present in the run products, and they can be at least partly attributed to carbon contamination during sample preparation for infrared analysis.

Run products were euhedral or subhedral crystals of silicates (or spinel) free of inclusions and visible impurities (Fig. 2), embedded in a fine-grained matrix of carbonates, representing quenched carbonatite melt. The grain size varied from ~ 30 μm to a few hundred micrometers. The growth of large crystals was probably enhanced by the presence of carbonate, which can act as a fluxing agent.

Carbonates were removed by etching with nitric or hydrochloric acid. Mineral phases were identified using X-ray powder diffraction and Raman spectroscopy. Carbon contents in synthesized minerals were measured with secondary ion mass spectroscopy (SIMS).

For use as SIMS blanks, we also synthesized large (up to 1 mm) homogeneous carbon-free crystals of enstatite (modified flux growth method of Ito [38], with carbon-free

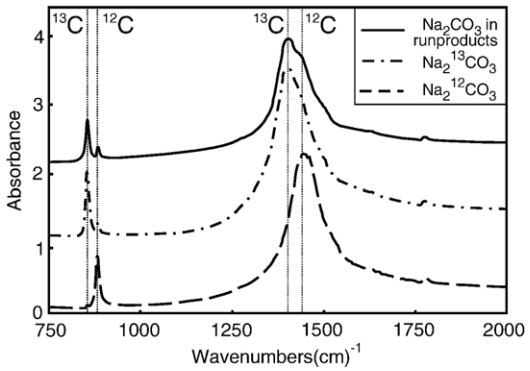

Fig. 1. Infrared spectra (KBr pellets) of isotopically "normal" Na_2CO_3 ($^{12}C/^{13}C \approx 89.9$) of Na_2CO_3 certified to contain 99% of the isotope ^{13}C and of the carbonate recovered from a piston cylinder experiment. The samples rich in ^{13}C probably exchanged some carbon dioxide with the air during preparation of the KBr pellet.

starting materials), diopside (direct crystallization in air from molten stoichiometric oxide mixture), pyrope (synthesis in piston cylinder at 3.5 GPa and 1100 °C) and three tholeiite glasses, doped with known amount of ^{13}C. The tholeiite glasses were synthesized from carbon-free glasses and known amounts of $Ag_2^{13}C_2O_4$ in piston cylinder experiments at 1.5 GPa and 1450 °C with a duration of 3 h. Compositions are given in Table 1. Carbon contents are believed to be accurate to 5% relative or better.

3. Analytical procedure

3.1. Sample preparation

The synthesized ^{13}C-saturated crystals were mounted on 2.5-cm-diameter round glass slides using a small amount of carbon-free ceramic glue (a hydrous solution of alkali silicate). The samples were subsequently dried for 1 day in air at 70 °C to remove absorbed water. Crystals were polished to produce a flat surface which stood, at most, a few tens of micrometers above the surface of the glass slide. Care was taken to make sure that good contact was established between the crystal edges and the glue, such that charge conduction during subsequent SIMS analysis would be assured. This method of preparing the samples was found to give the best results; however, it also had the drawback of the glue losing its integrity on some samples if they had been exposed to air for several weeks.

3.2. Reference materials

SIMS is a comparative technique, and for quantification of measured carbon, calibration samples are

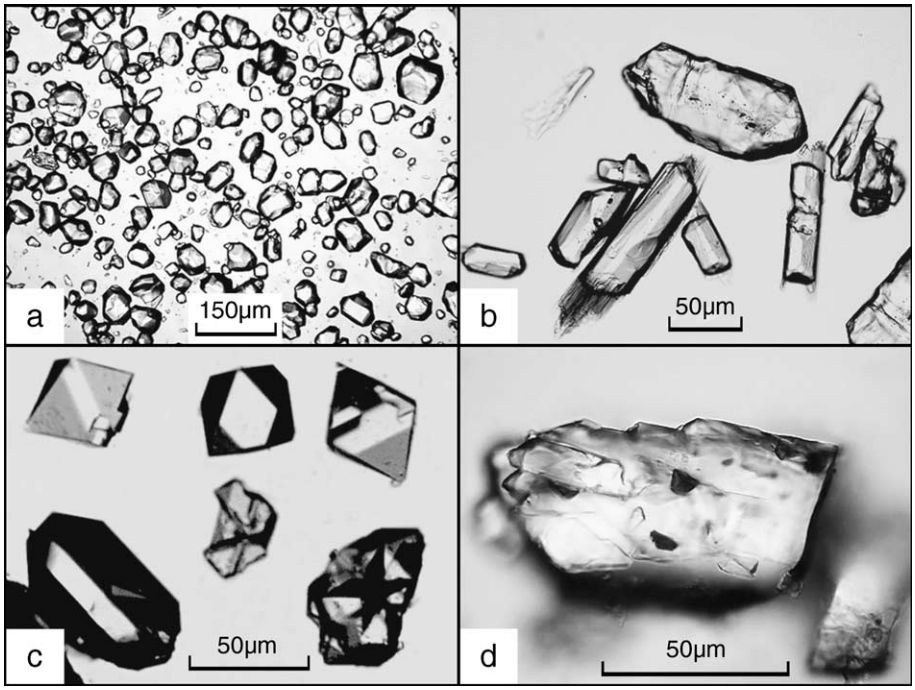

Fig. 2. Optical micrograph of run products after removal of carbonates; (a) olivine, (b) enstatite, (c) $MgAl_2O_4$–spinel, (d) $MgSiO_3$–ilmenite.

necessary. The main limitation of SIMS is that ion yields are extremely dependent on the matrix of the sample. In order to have matrix-matched reference materials, synthesized nominally carbon-free crystals of olivine, enstatite, diopside and pyrope were prepared on mounts as described above. Additionally, a commercially purchased large, single-crystal spinel was cut into three 7.5×7.5-mm plates. All of these crystals were polished to a sample surface roughness of ~ 10 nm using an ethanol-based slurry of polycrystalline diamond powder on Al foil. These samples were cleaned in high-purity ethanol, were dried in air at ~ 70 °C to evaporate all ethanol and were then sent for commercial ion implantation (Panalytic GmbH, Dresden). Thermally decomposed $Na_2^{13}CO_3$ was used as a source material for the 60 kV implantation of a known dose ($3\times10^{14}\pm3\%$ At/cm^2) of ^{13}C.

Table 1
Relative sensitivity factors (RSF) of various reference materials

Mineral	Measured ratio	RSF	Number of measurements
Tholeiite glasses [a] (^{13}C-doped, synthetic)	^{13}C/^{28}Si	0.297±0.055	6
Spurrite [b] (natural)	^{13}C/^{28}Si	0.421±0.062	25
Forsterite (^{13}C-implanted, synthetic)	^{13}C/^{28}Si	0.411±0.025	6
Enstatite (^{13}C-implanted, synthetic)	^{13}C/^{28}Si	0.753±0.031	3
Diopside (^{13}C-implanted, synthetic)	^{13}C/^{28}Si	0.707±0.023	3
Pyrope (^{13}C-implanted, synthetic)	^{13}C/^{28}Si	0.810±0.039	3
Spinel (^{13}C-implanted, synthetic)	^{13}C/^{27}Al	3.498±0.161	3

Errors are one standard deviation.
[a] Composition: 60.5 wt.% SiO_2, 2 wt.%TiO_2, 14.5 wt.% Al_2O_3, 9.9 wt.% MgO, 8.8 wt.% CaO, 3.3 wt.% Na_2O, 1.6 wt.% K_2O, doped with 793, 1484, and 3130 ppm of ^{13}C.
[b] Natural samples from New Mexico (USA) and Durango (Mexico).

Ion implantation was not feasible for minerals of the transition zone and lower mantle as this procedure would most likely convert these metastable phases to amorphous material. Synthetic tholeiite glasses doped with a known amount of ^{13}C were used as reference materials instead. The concentration of carbon in these samples was calculated from composition of the starting mixture.

The natural ratio of carbon isotopes, required to estimate isotope fractionation during analysis, was calibrated using two natural spurrite ($Ca_5CO_3(SiO_4)_2$) specimens from Durango, Mexico, and New Mexico, USA.

3.3. Analytical conditions

SIMS analyses were conducted on the Cameca ims 6f at the GeoForschungsZentrum Potsdam. This instrument

had been modified from its original design such that all pumps operated oil-free. In order to suppress outgassing of the samples, the mounts were stored for at least 24 h in an in-house designed UHV sample storage chamber [39]. Further vacuum improvements (by a factor of about 3×) were achieved by using a liquid nitrogen cold trap, such that the source operating pressure of the instrument was on the order of 1×10^{-7} Pa when samples were present.

Each of the ^{13}C-saturated samples was cleaned in ethanol, dried, and coated with between 50 and 80 nm of high-purity gold. The actual SIMS analyses employed a nominally 12.5 kV, 1–2 nA $^{133}Cs^{+}$ beam, which was focused to a ~ 5×8-μm spot on the sample surface. In order to reduce the impact of surface carbon contamination, each domain which was to be analyzed was pre-sputtered with a 25×25-μm rastered beam for 3 min before beginning the actual analysis. Furthermore, as a part of the analysis, a 3-min spot preburn was conducted in order to establish equilibrium sputtering conditions. Charge compensation employed a normal incidence electron flood gun operated at the same voltage as the sample stage.

The secondary side of the SIMS was operated at a mass resolving power of $M/\Delta M \approx 4300$ which over-resolved the $^{12}CH^{-}$ interference from the lighter $^{13}C^{-}$ mass position. The carbon signal derived from any surface contamination sputtered by stray neutral primary atoms was suppressed from the mass spectrum by employing a 400-μm field aperture which was equivalent to a 30-μm field-of-view at the sample surface. The actual analyses employed 20 cycles of the following peak stepping sequence 11.5 background (0.1 s per cycle), ^{12}C (4 s), ^{13}C (15 s) and ^{28}Si (4 s) (or alternatively ^{27}Al in the case of spinel).

3.4. Calculations

Despite all of the efforts described above, laboratory contamination was a major source of carbon in our analyses. Nevertheless, unlike samples with a natural isotopic composition (spurrite; $^{13}C^{-}/^{12}C^{-}=0.011\pm1.4\%$, $n=25$), the synthetic crystals showed elevated $^{13}C^{-}/^{12}C^{-}$ ratios of up to 0.3. Since the crystals were saturated with the rare isotope ^{13}C, the amount of carbon contamination could be quantified, assuming that it has a natural $^{13}C/^{12}C$ ratio. Therefore, the "true" absolute concentration of the ^{13}C dissolved in carbon-saturated silicates could be established, despite significant laboratory C contributions, by measuring $^{13}C^{-}/^{28}Si^{-}$ and $^{12}C^{-}/^{13}C^{-}$ ratios in conjunction with both the known isotopic signature of the extraneous carbon and the C/Si relative sensitivity factor (RSF) obtained from the reference samples. An identical approach, based on ^{27}Al, was used for calculating the carbon content in spinel.

To determine the RSF for each upper mantle mineral, we conducted multiple depth profiles on the implanted reference samples. SIMS depth profiles used parameters similar to those employed during the analysis of the synthesized crystals, the main difference being that data were collected with an 80×80-μm raster. In order to eliminate contamination from the crater walls, the beam was centred under the field aperture using the scanning ion image capability of the Cameca ims 6f. After an initial pulse of carbon derived from surface contamination, an excess in ^{13}C well above the natural isotopic composition was clearly detected. To eliminate the impact of the extraneous surface carbon, we only used those data collected after two cycles subsequent to the penetration of the gold coat when a precipitous drop in the reference isotope (^{28}Si or ^{27}Al) was observed. The data from the depth profile, including a correction for the extraneous ^{12}C-rich carbon, were converted into the required RSF (Table 1) using the formula:

$$RSF = \frac{\left(mean^{13}C^{-}_{cps} \Big/ mean^{28}Si^{-}_{cps}\right)_{measured}}{\left(flux^{13}C \Big/ (depth\cdot\rho\cdot Si_{wt\%}\cdot(N_A/At_{wt}Si)\cdot(at^{28}Si/Si_{total}))\right)},$$

where flux^{13}C is implanted dose of ^{13}C, depth is crater depth, ρ and $Si_{wt.\%}$ are density and weight percent of Si (Al for spinel) in the analyzed mineral respectively, N_A is Avogadro's number, $At_{wt}Si$ is atomic weight of silicon (28.08 g/mol); $at^{28}Si/Si_{total}$ is mole fraction of ^{28}Si (0.922). Crater depths, typically on the order of 300 nm deep, were determined with a Dektak3 stylus profilometer which is accurate to better than ±2%. The external reproducibility of this method for determining the RSF is estimated to be of the order of 2.4–4.8%.

For wadsleyite, ringwoodite, $MgSiO_3$–ilmenite and $MgSiO_3$–perovskite, we used a different approach for defining the RSF. Three synthetic tholeiite glasses were used to determine a calibration curve for which the best-fit line of the 18 analyses was forced through the origin and the slope of this line was used to determine the RSF for these minerals. The external precision of this method was ±13.9% (1σ). In view of the potential impact of using non-matrix-matched reference samples, the accuracy of the quantitative results for the minerals of the transition zone and lower mantle is potentially not as good as those obtained for the upper mantle minerals. However, as it turned out during the course of this study, no carbon could be detected in these phases anyway.

Table 2
Experimental data on carbon solubility in upper mantle minerals

Run	Mineral	T (°C)	P (GPa)	Log (fO_2)	t (h)	C content[a] (wt. ppm)
Ol9	Forsterite	900	1.5	Not buffered	144	0.38±0.09 0.29±0.07
Ol10	Forsterite	1000	1.5	Not buffered	168	0.12±0.03 0.10±0.03
Ol11	Forsterite	1100	1.5	Not buffered	144	<0.09[b] 0.10±0.03
Ol-11F2	Olivine[c]	1100	1.5	Not buffered	144	0.21±0.06 0.20±0.03
Ol-11F3	Olivine[c]	1100	1.5	Not buffered	144	0.34±0.02 0.30±0.03
MA-Ol-7	Forsterite	1200	7	Not buffered	10	3.90±0.68 3.27±0.29 3.53±0.43
MA-Ol-11	Forsterite	1200	11	Not buffered	10	12.75±0.53 11.57±0.34 11.59±1.04
Ol-11F1	Olivine[c]	1100	1.5	−12.7	96	0.52±0.06 <0.04[b] <0.07[b]
Ol-11C	Olivine[c]	1100	1.5	−10	96	0.29±0.08 0.22±0.06
Ol-11N	Olivine[c]	1100	1.5	−8.2	96	0.34±0.12
E9	Enstatite	900	1.5	Not buffered	96	0.07±0.01 0.14±0.02 0.15±0.02
E10	Enstatite	1000	1.5	Not buffered	96	0.19±0.04 0.05±0.01 0.07±0.01
E11	Enstatite	1100	1.5	Not buffered	168	0.06±0.01 0.05±0.01 0.10±0.01
MA-E-6	Enstatite	1100	6	Not buffered	5	0.44±0.03 0.38±0.03 0.30±0.02
MA-W-16	Enstatite	1400	16	Not buffered	10	0.69±0.06 0.65±0.04 0.80±0.06
D9	Diopside	900	1.5	Not buffered	168	<0.01[b] 0.02±0.01
D10	Diopside	1000	1.5	Not buffered	96	0.12±0.01 0.10±0.01 0.08±0.01
D11	Diopside	1100	1.5	Not buffered	96	0.16±0.02 0.09±0.01 0.07±0.01
MA-D-6	Diopside	1100	6	Not buffered	8	1.45±0.07 1.60±0.06 1.50±0.07
MA-Py-6	Pyrope	1300	6	Not buffered	10	0.85±0.05 0.87±0.05
MA-Py-9	Pyrope	1300	9	Not buffered	10	0.83±0.06 1.27±0.07 1.07±0.06
MA-Py-10	Pyrope	1300	10	Not buffered	6	0.82±0.04 0.96±0.05
Sp	Spinel	1100	1.5	Not buffered	168	<0.03[b] <0.02[b]

Table 1 compares relative sensitivity factors derived from the C-implanted crystals, tholeiite glasses and natural spurrite. The cause for the variability of the RSF for Si and C among silicates could not be established unambiguously. However, the variations are below a factor of three, despite the massive structural differences between the phases and despite variations in absolute carbon contents spanning many orders of magnitude.

For many of our analyses, we detected no excess ^{13}C, implying extremely low carbon solubility. The limit of detection for carbon for individual analyses calculated from the 3σ uncertainty in the measured isotopic ratios depends essentially on the carbon background and is in the range 30–200 ppbw.

4. Results

Experimental results are summarized in Tables 2 and 3. Only measurements with steady state count rates of sputtered carbon ions within the whole accumulation time were taken into account (Fig. 3). Although crystals were inspected with an optical microscope to assure the absence of inclusions prior to SIMS, several analyses yielded local carbon contents on the order of tens or hundreds of ppm of ^{13}C by weight (ppmw). Such high concentrations, which were observed only on certain spots of the respective samples, are attributed to carbon-rich inclusions or fractures in a host grain. Generally, a single carbonaceous impurity smaller than 1 μm will increase the count rate of ^{13}C at least by factor 8–10. Thus, any such inclusion-hosted carbon could be readily distinguished from dissolved carbon intrinsic to the crystal host.

4.1. Olivine

Olivine constitutes ~ 60% of the upper mantle by volume and could therefore represent a major carbon reservoir. Carbon solubility in olivine was measured as a function of pressure, temperature, redox conditions and mole fraction of fayalite. Clearly, the major factor controlling carbon dissolution in olivine is pressure

Notes to table:
Runs with prefix "MA" were carried out in the multi-anvil press, all other experiments were performed in a piston cylinder apparatus. Errors are one standard deviation.
[a] If several numbers are given, they represent analysis of different crystals in the charge.
[b] Values are below limit of detection.
[c] For composition see Table 4.

Table 3
Experimental data on carbon solubility in minerals of the transition zone and lower mantle

Run	Mineral	T (°C)	P (GPa)	t (h)	C content[a] (wt. ppm)
MA-W-16	Wadsleyite	1400	16	10	0.04±0.01
					<0.04[b]
MA-W-17	Wadsleyite	1400	17	4	<0.07[b]
					<0.05[b]
MA-R-21	Ringwoodite	1200	21	10	0.04±0.01
MA-R-23	Ringwoodite	1200	23	4	0.10±0.02
					<0.07[b]
					<0.08[b]
MA-I-25	Mg–Ilmenite	1400	25	10	<0.10[b]
					<0.08[b]
					<0.11[b]
MA-Ps-25	Mg–Perovskite	1400	25	10	<0.10[b]
					<0.07[b]
					<0.09[b]
					<0.10[b]
MA-Ps-26	Mg–Perovskite	1400	26	3	<0.05[b]
					<0.09[b]

All experiments were conducted in a multi-anvil press.
Errors are one standard deviation.
[a] Each number refers to the analysis of one single crystal in the charge.
[b] Values are below limit of detection.

(Table 2, Fig. 4). Carbon solubility in pure forsterite increases exponentially by two orders of magnitude when pressure rises from 1 to 11 GPa, but even at the highest pressures studied, the solubility reaches only 12 ppmw. Experiments performed at a given pressure but at different temperatures (900–1100 °C) show no systematic effect. Similarly, varying the oxygen fugacity over several orders of magnitude from Fe–FeO to Ni–NiO buffer conditions did not significantly affect carbon solubility in olivine. It should be noted

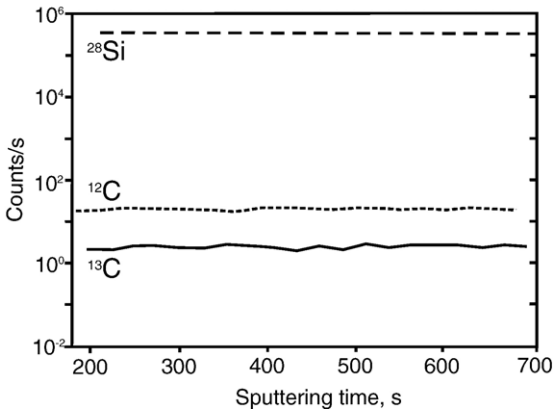

Fig. 3. Example of count rates of ions sputtered from C-saturated crystals as a function of time. Run MA-D-6.

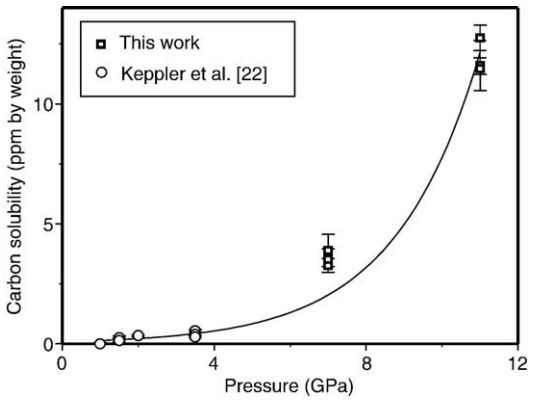

Fig. 4. Carbon solubility in forsterite as a function of pressure for T=1200 °C. Error bars are one standard deviation. The curve shown is a best fit of the experimental data by an equation of the form $C=A\exp(-P\Delta V/(RT))$ with A=0.089 ppmw and ΔV=−5.47 cm^3/mol.

that the use of Fe, Co and Ni as capsule material resulted in the incorporation of these elements in the synthesized olivine (Table 4). For the Co- and Ni-bearing samples, no significant change in ion yield was observed, but the observed SIMS ion count rate of Si slightly increased for olivine with the highest Fe-content (run Ol-11F1 in Table 4). Similar matrix effects, associated with Fe-bearing minerals, have been documented in previous studies ([40] and references therein). The cause of these effects is poorly understood; probably iron reduces the strength of Si bonds in olivine. Thus, the carbon solubility in Fe-bearing olivine might be underestimated by factor of 1.5–2, because the RSF were all calibrated against a pure forsterite reference material. However, no significance influence of the fayalite component on carbon solubility is detectable, even if the data in Table 2 (runs Ol-11F1-Ol-11F3) were corrected according to the elevated ion yield of Si.

4.2. Pyroxenes

Pyroxenes account for 25 vol.% of the upper mantle. Although they were suggested to dissolve more carbon than olivine [41,42], we observed a pattern of

Table 4
Composition of olivine doped with Fe, Ni and Co

Run	Formula
Ol-11N (Ni-capsule)	$Mg_{1.977}Ni_{0.032}Si_{0.995}O_4$
Ol-11C (Co-capsule)	$Mg_{1.850}Co_{0.165}Si_{0.993}O_4$
Ol-11F1 (Fe-capsule)	$Mg_{1.761}Fe_{0.248}Si_{0.996}O_4$
Ol-11F2 (5% Fa in starting mixture)	$Mg_{1.945}Fe_{0.062}Si_{0.997}O_4$
Ol-11F3 (10% Fa in starting mixture)	$Mg_{1.887}Fe_{0.122}Si_{0.995}O_4$

Compositions were obtained by electron microprobe.

carbon solubility essentially similar to that of olivine for both enstatite and diopside (Table 2, Fig. 5). At lower pressure (1.5 GPa) both minerals show a solubility of less than 200 ppbw, which is approximately one order of magnitude lower than recently reported [22] and close to the limit of detection of our technique. Pyroxene crystals grown at higher pressure dissolved more carbon, but the amount remains less than that of olivine (Fig. 5). Enstatite, coexisting with wadsleyite, was recovered from an experiment at 16 GPa (MA-W-16 in Table 2). According to the $MgSiO_3$ phase diagram (e.g., [43]), high-clinoenstatite rather than orthoenstatite is stable at pressures higher than 8–9 GPa, but it readily transforms to enstatite upon decompression.

4.3. Pyrope

Pyrope constitutes about 15 vol.% of the upper mantle. Its fraction increases with depth due to solid solution with pyroxenes. Carbon solubility in pyrope increases with pressure as in olivine, but the pressure dependence is weaker (Table 2, Fig. 5).

4.4. Spinel

$MgAl_2O_4$ spinel is stable only in the uppermost mantle. We failed to detect any carbon in $MgAl_2O_4$ spinel above the detection limit of ~ 30 ppb by weight.

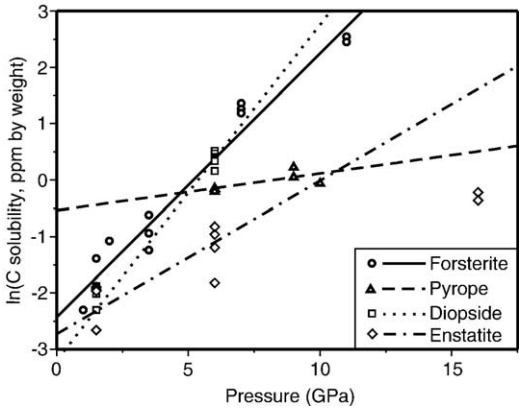

Fig. 5. Plot of the logarithm of carbon solubility in upper mantle silicates versus pressure for T=900–1200 °C. The slopes of the lines are related to the volume change ΔV of the dissolution reaction according to $d\ln K/dP = -\Delta V/RT$, where K is the equilibrium constant proportional to carbon solubility, R is the ideal gas constant and T is temperature. Estimated values of ΔV are −5.47 cm^3/mol for forsterite, −3.0 cm^3/mol for enstatite, −6.4 cm^3/mol for diopside and −0.9 cm^3/mol for pyrope. Except for forsterite, these data are, however, only constrained by a few measurement and they may therefore be subject to substantial errors.

4.5. Transition zone and lower mantle minerals

The first experimental results on carbon solubility in major minerals of the transition zone and lower mantle are summarized in Table 3. Most of the synthesized crystals show no excess of the ^{13}C isotope relatively to the natural ratio of $^{13}C/^{12}C$. Therefore, we conclude that the maximum carbon solubility in wadsleyite, ringwoodite, $MgSiO_3$–ilmenite and $MgSiO_3$–perovskite is below our limit of detection of 40–110 ppbw. Since these numbers were obtained by using non-matrix matched tholeiite glass reference samples, systematic errors of up to a factor of 2–3 cannot be excluded. RSFs calculated for crystalline phases in this study are higher than that for glass (Table 1); therefore, it is suggested that the ionization of carbon relative to silicon is higher for a crystalline matrix than for an amorphous material. In this case, the detection limits of carbon would be even lower.

5. Discussion: carbon speciation in silicates

In spite of extensive studies during the past 40 yr, there is no consensus on the potential mechanism of carbon incorporation in silicates. Neutral carbon has been suggested to dissolve interstitially or in cation vacancies [44]. Fyfe [45], Ernst et al. [46] and Ernst and Schwab [47] suggested that carbon may directly substitute for silicon in tetrahedral coordination; they even speculated about a solid solution of "orthocarbonates" with silicates. The exceedingly low carbon solubility in silicates documented in this study suggests that direct study of carbon speciation by spectroscopic methods is impossible. However, the analysis of the thermodynamic data provides some insight into speciation. In particular, the observation that carbon solubility in olivine is independent of oxygen fugacity is quite significant.

Carbon in carbonates is in the +4 oxidation state. If it was incorporated in minerals in any other form than C^{4+}, redox exchange reactions would be involved. For example, the reaction

$$C^{4+}_{carbonate} + 2O^{2-}_{mineral} \rightarrow C^{0}_{mineral} + O_2$$

describes the dissolution of carbon in neutral form with the equilibrium constant

$$K = \frac{[C^{0}_{mineral}] \cdot f_{O_2}}{[C^{4+}_{carbonate}] \cdot [O^{2-}_{mineral}]^2}.$$

Consequently, one would expect carbon solubility to decrease with oxygen fugacity according to

$$[C^0_{mineral}] \sim \frac{1}{f_{O_2}}.$$

The expected dependencies of carbon solubility on oxygen fugacity for different substitution mechanisms are plotted in Fig. 6 together with the experimental data for olivine. In these experiments, carbon was only present as carbonate; no evidence for the presence of reduced carbonaceous material was seen. Evidently, the experimental data exclude the possibility of a change in oxidation state of carbon during dissolution. Therefore, carbon in olivine must be dissolved as C^{4+}. This leaves two possibilities. Either C^{4+} directly substitutes for Si^{4+}, or C^{4+} may occupy interstitial sites. Considering the small ionic radius of C^{4+} (15 pm, [48]) the latter possibility would appear to be quite reasonable. However, the systematic variations in carbon solubility observed for different minerals rather suggest the direct substitution of C^{4+} for Si^{4+}, as the solubility is clearly correlated with the volume of the Si^{4+} site in the respective minerals. While the Si–O bond length in tetrahedra does not differ much among common upper mantle silicates, the tetrahedral volumes vary more notably. Moreover, polyhedral volumes are more sensitive to compression because of deviation of (1) bond angle strain, (2) polyhedral angle variance, and (3) mean polyhedral elongation [49]. Fig. 7 gives a plot of carbon solubility vs. the volume of the Si tetrahedron (i.e., the tetrahedron defined by the centres of the four oxygen atoms surrounding the Si atom) in the respective structures [50,51].

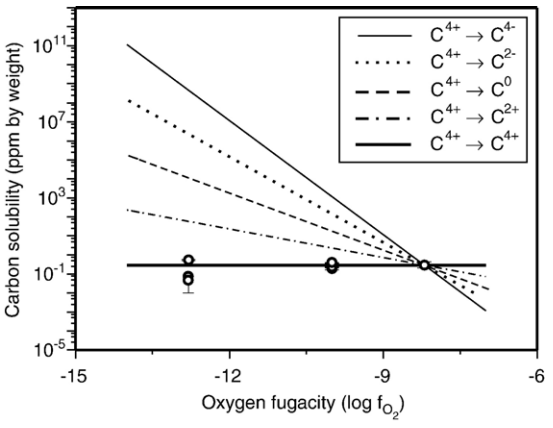

Fig. 6. Dependence of carbon solubility in olivine on oxygen fugacity at 1.5 GPa and 1100 °C. Theoretical slopes for different solution mechanisms are shown for comparison.

Fig. 7 describes perfectly the variations of carbon solubility among upper mantle silicates as well as the failure to find any carbon in wadsleyite and ringwoodite. Silicon in $MgSiO_3$–ilmenite and $MgSiO_3$–perovskite is in octahedral coordination. This site, still being the smallest in their structures, has a much longer Si–O bond and larger polyhedral volume (e.g., 7.68 $Å^3$ in perovskite compared to 2.10–2.24 $Å^3$ in upper mantle minerals), in agreement with the increase of interatomic distances with increasing coordination number [52]. The smallest polyhedra in $MgAl_2O_4$ spinel are MgO_4 tetrahedra with a volume in the range of 3.653–3.827 $Å^3$. It is therefore not surprising that no carbon was detected in $MgAl_2O_4$ spinel. Fig. 7 is also consistent with our observation that the substitution of Mg by Fe (or Co or Ni) in olivine does not affect carbon solubility, because the volume of the SiO_4 tetrahedron does not vary significantly even among the end-members forsterite, fayalite, liebenbergite and Co-olivine.

The correlation shown in Fig. 7 can be used to estimate carbon solubility in other silicates. Those with larger polyhedral volumes, (e.g., Ca-garnet (2.255 $Å^3$)) would dissolve virtually no carbon, while the smaller volume of the SiO_4 tetrahedron in zircon (2.118 $Å^3$) and plagioclase (2.12–2.15 $Å^3$) should show enhance carbon solubility. However, due to their low abundance or limited stability field in the mantle, these minerals are unlikely to be significant reservoirs of carbon.

The fact that in some of the multi-anvil experiments some traces of carbonaceous material were observed implies that the minerals grown in these experiments were also in equilibrium with some reduced carbon species. The precise nature of the carbonaceous material is not known and it may well be material precipitated from a fluid phase during quenching. However, the fact that no anomalies in carbon solubility were observed in these experiments suggest that carbon solubility in mantle minerals does not change by orders of magnitude if these minerals are in equilibrium with some reduced carbon species rather than with carbonates.

6. Implications for carbon storage in the mantle

The geological implications of this study are strongly dependent on estimates of the bulk carbon content of the mantle. Direct measurements on xenoliths and other mantle-derived samples yielded concentrations from below 1 ppmw to almost 10,000 ppmw (e.g., Fig. 3 in [53] and references therein), which may suggest either a highly heterogeneous distribution of carbon in the mantle source or different degrees of carbonate survival during transfer to the surface [54,55]. Values for the

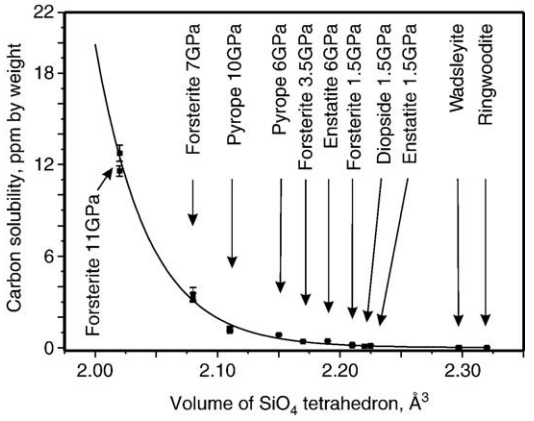

Fig. 7. Carbon solubility in silicates as a function of the volume of the SiO_4 tetrahedron. Volume data are from [50,51] and references therein. The curve shown is a guide for the eye only.

oceanic upper mantle range from 20 to 1000 ppmw C, as derived from studies of MORB glasses [56], undersaturated melt inclusions in olivine phenocrysts [22], mass balance of volcanic gas emissions [57–59] and rare gas systematic [60,61]. Cosmochemical estimates based on ratios of elements with similar volatility as carbon (for instance, $C/^{36}Ar$ [1], or $C/^{3}He$, [62]) in chondrites generally suggest rather high carbon abundances in the bulk Earth of the order of 1000 ppm or higher, with most of this carbon presumably residing in the mantle.

If such values are compared to the carbon solubilities established in this study, it is obvious that across much of the mantle most of the carbon must be stored in a separate carbon-rich phase. This could either be a carbonate phase or elemental carbon in the form of graphite or diamond. Estimates of carbon abundance in the upper mantle, although somewhat uncertain, usually range from 100 to more than 1000 ppm, implying that diamond would have to be a common accessory mineral in mantle xenoliths coming from the diamond stability field, if carbon was present as a pure element. This does not agree with the observation that diamond is an exceedingly rare mineral. Therefore, it is almost certain that carbonates (i.e., dolomite or magnesite) are the main storage sites of carbon throughout most of the upper mantle [23–25,63]. Considering the low melting point of carbonates [64] and the low viscosity of carbonatite melts [65] which form close to the solidus of a carbonated mantle, it would be very surprising if carbon were homogeneously distributed in the mantle. Rather, since the mantle geotherm is close to or above the solidus of carbonated peridotite throughout much of the deeper upper mantle, local carbon enrichment due to carbonatite melts should be common. Unfortunately, the density of anhydrous and hydrous carbonatite melts is not known under the relevant conditions of pressure and temperature, and therefore, it is not possible to predict whether carbonatite melts would tend to rise or to descend in a carbonated mantle. If these melts were less dense than the surrounding peridotite, in agreement with measurements at 1 bar [65], one could imagine a continuous enrichment of the shallow mantle by carbonatite melts generated during mantle convection. These melts would percolate upward through the mantle until they solidify as the mantle geotherm intersects the solidus. In this way, massive carbonate enrichments could be generated, particularly in the shallow mantle below old, cold and stable continental crust. This idea is entirely consistent with the widely seen enrichment of CO_2 in magmas originating in the subcontinental mantle [66]. It is intriguing to speculate that large shallow carbonate enrichments could be tapped by continental flood basalts with the effect of a sudden injection of large amounts of carbon dioxide into the atmosphere, possibly triggering mass extinctions. At least for the Triassic–Jurassic boundary, which coincides with the activity of the central Atlantic magmatic province, stomatal indices in fossil ginkgo leaves suggest a sudden rise in atmospheric CO_2 right at the boundary [67]. Moreover, most flood basalt provinces that coincide with extinction events appear to be correlated with global warming, oceanic anoxia and sometimes a calcification crisis, which are all pointing towards sharply increased atmospheric CO_2 levels [68].

If the curve for olivine in Fig. 4 is extrapolated to the base of the upper mantle at a depth of ~ 410 km, carbon

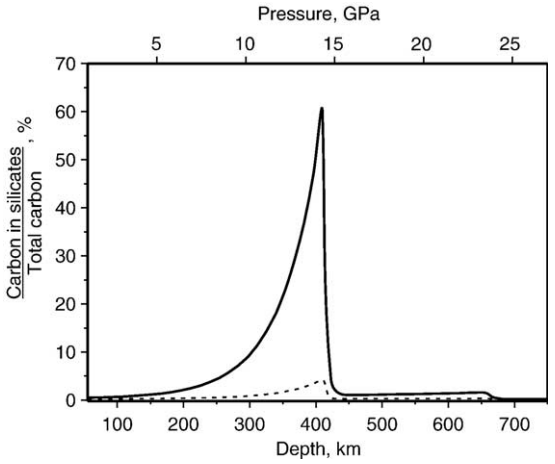

Fig. 8. Fraction of total mantle carbon, dissolved in silicates as a function of depth for a depleted MORB source (73 ppmw C, [61], solid line) and for fertile pyrolitic mantle (1000 ppmw, [5], dotted line). The curves were calculated from the experimental solubility data reported in this study and assuming a pyrolitic mineral assemblage of the mantle.

solubility in olivine reaches 45–50 ppmw. This value is still much smaller than the 1000 ppm often assumed for a fertile mantle peridotite, but it is comparable to some of the lowest values derived for bulk carbon concentration in depleted mantle [22,61]. Accordingly, for a depleted mantle source composition, there might be a narrow layer just above the transition zone where most of the carbon is stored in olivine (Fig. 8). Upon subduction or downwelling of such a depleted carbon reservoir, carbonate, probably in the form of a carbonatite melt, will exsolve once the reservoir passes through the olivine to wadsleyite transformation. The geodynamic significance of this effect entirely depends on the density contrast between carbonate melt and surrounding peridotite. If the melt is denser than the peridotite, it will continue to descend into the deeper mantle. However, if the melt were still less dense than the surrounding peridotite, it could percolate upward while the residual peridotite may continue to descend into the lower mantle. In this case, a situation would arise that is in some ways similar to the water filter model proposed by Bercovici and Karato [69], but with quite the opposite effect. While the Bercovici and Karato model is a mechanism to retain incompatible elements in the lower mantle, the formation of a carbonatite melt of low density at the 410-km discontinuity could retain CO_2 in the upper mantle and prevent is from being recycled into the lower mantle. However, the geodynamic significance of this effect is uncertain, as it would only be relevant for carbon-depleted reservoirs.

While carbonate is the most plausible host for carbon in upper mantle [25,64], changes in ambient oxygen fugacity may stabilize diamond in the transition zone and lower mantle [21,34,70–73]. However, the redox equilibria between carbonate and diamond are not well studied under the relevant conditions of pressure and temperature. In any case our study clearly demonstrates that most of the carbon in the mantle of Earth, Mars and Venus must be stored in a separate phase. Due to the lower pressures in the mantle of Mars, the solubility of carbon in the minerals of the upper part of the Martian mantle will be even lower than on Earth.

Acknowledgements

This study was supported by German Science Foundation (Leibniz award to HK). Comments from two anonymous referees improved the manuscript.

References

[1] W. Otting, J. Zahringer, Total carbon content and primordial rare gases in chondrites, Geochim. Cosmochim. Acta 31 (1967) 1949–1960.

[2] E. Anders, T. Owen, Mars and Earth; origin and abundance of volatiles, Science 198 (1977) 453–465.

[3] H.P. Scott, Q. Williams, E. Knittle, Stability and equation of state of Fe_3C to 73 GPa: implications for carbon in the Earth's core, Geophys. Res. Lett. 28 (2001) 1875–1878.

[4] B.J. Wood, Carbon in the core, Earth Planet. Sci. Lett. 117 (1993) 593–607.

[5] A. Jambon, Earth degassing and large-scale geochemical cycling of volatile elements, Rev. Miner. 30 (1994) 479–517.

[6] R. Luth, Mantle volatiles—distribution and consequences, in: R.W. Carlson (Ed.), Treatise on Geochemisrty, vol. 2, 2003, pp. 319–361.

[7] D. Brewster, On the existence of two new fluids in the cavities of minerals, which are immiscible, and possess remarkable physical properties, Philos. J. 9 (1823) 94–95, 268–270.

[8] H. Vogelsang, Nachtrag zu der Abhandlung "Über Flüssigkeitseinschlüsse in Gestein", Ann. Phys. Chem. 137 (1869) 257–271.

[9] H. Vogelsang, H. Geissler, Über die Natur der Flüssigkeitseinschlüsse in gewissen Mineralien, Ann. Phys. Chem. 137 (1869) 56–74.

[10] H.W. Green, A CO_2 charged asthenosphere, Nature 238 (1972) 2–5.

[11] H.W. Green, Y. Guegen, Origin of kimberlite pipes by diapiric upwelling in the upper mantle, Nature 249 (1974) 617–620.

[12] E. Roedder, Fluid inclusions, Min. Soc. Am. (1984). 644 pp.

[13] E. Roedder, Liquid CO_2 inclusions in olivine-bearing nodules and phenocrysts from basalts, Am. Mineral. 50 (1965) 1746–1782.

[14] T. Ernst, R.G. Schwab, B. Scheubel, P. Brosch, High pressure experiments on the equilibrium olivine–CO_2–enstatite–carbonate in natural system, in: W. Schreyer (Ed.), High Pressure in Geosciences, 1982.

[15] D. Canil, H.S.C. O'Neill, D.G. Pearson, R.L. Rudnick, W.F. McDonough, D.A. Carswell, Ferric iron in peridotites and mantle oxidation states, Earth Planet. Sci. Lett. 123 (1994) 205–220.

[16] A.E. Saal, E.H. Hauri, C.H. Langmuir, M.R. Perfit, Vapour undersaturation in primitive mid-ocean-ridge basalt and the volatile content of Earth's upper mantle, Nature 419 (2002) 451–455.

[17] T.N. Tingle, H.W. Green, A.A. Finnerty, Experiments and observations bearing on the solubility and diffusivity of carbon in olivine, J. Geophys. Res. 93 (1988) 15289–15304.

[18] I.S.T. Tsong, U. Knipping, Comment on "Solute carbon and carbon segregation in magnesium oxide single crystals; a secondary ion mass spectrometry study" by F. Freund; discussion, Phys. Chem. Miner. 13 (1986) 277–279.

[19] I.S.T. Tsong, U. Knipping, C.M. Loxton, C.W. Magee, G.W. Arnold, Carbon on surfaces of magnesium oxide and olivine single crystals; diffusion from the bulk or surface contamination? Phys. Chem. Miner. 12 (1985) 261–270.

[20] F. Freund, H.W. Kathrein, H., R. Knobel, H.J. Heinen, Carbon in solid solution in forsterite; a key to the untracable nature of reduced carbon in terrestrial and cosmogenic rocks, Geochim. Cosmochim. Acta 44 (1980) 1319–1334.

[21] E.A. Mathez, J.D. Blacic, J. Beery, M. Hollander, C. Maggiore, Carbon in olivine; results from nuclear reaction analysis, J. Geophys. Res. 92 (1987) 3500–3506.

[22] H. Keppler, M. Wiedenbeck, S.S. Shcheka, Carbon solubility in olivine and the mode of carbon storage in the Earth's mantle, Nature 424 (2003) 414–416.

[23] C. Biellmann, P. Gillet, F. Guyot, J. Peyronneau, B. Reynard, Experimental evidence for carbonate stability in the Earth's lower mantle, Earth Planet. Sci. Lett. 118 (1993) 31–41.

[24] M. Isshiki, T. Irifune, K. Hirose, S. Ono, Y. Ohishi, T. Watanuki, E. Nishibori, M. Takata, M. Sakata, Stability of magnesite and its high-pressure form in the lowermost mantle, Nature 427 (2004) 60–63.
[25] A. Wang, J.D. Pasteris, H.O.A. Meyer, M.L. Dele-Duboi, Magnesite-bearing inclusion assemblage in natural diamond, Earth Planet. Sci. Lett. 141 (1996) 293–306.
[26] T. Stachel, G.P. Brey, J.W. Harris, Inclusions in sublithospheric diamonds: glimpses of deep Earth, Elements 1 (2005) 73–78.
[27] C. McCammon, Deep diamond mysteries, Science 293 (2001) 813–814.
[28] W. Johannes, Eine vereinfachte Piston-Zylinder-Apparatur hoher Genauigkeit, N. Jb. Miner. 1973 (1973) 337–351.
[29] F. Schilling, B. Wunder, Temperature distribution in piston-cylinder assemblies: Numerical simulations and laboratory experiments, Eur. J. Miner. 16 (2004) 7–14.
[30] D.C. Rubie, S. Karato, H. Yan, H.S.C. O'Neill, Low differential stress and controlled chemical environment in multi-anvil high-pressure experiments, Phys. Chem. Miner. 20 (1993) 315–322.
[31] Y. Fei, S.K. Saxena, A. Navrotsky, Internally consistent thermodynamic data and equilibrium phase relations for compounds in the system MgO–SiO_2 at high pressure and high temperature, J. Geophys. Res. 95 (1990) 6915–6928.
[32] D.J. Frost, F. Langenhorst, P.A. van Aken, Fe–Mg partitioning between ringwoodite and magnesiowustite and the effect of pressure, temperature and oxygen fugacity, Phys. Chem. Miner. 28 (2001) 455–470.
[33] D.H. Eggler, D.R. Baker, Reduced volatiles in the system C–O–H; implications to mantle melting, fluid formation, and diamond genesis, in: S. Akimoto, M.H. Manghnani (Eds.), High pressure research in geophysics, 1982, pp. 237–250.
[34] R. Luth, Carbon and carbonates in the mantle, in: Y. Fei, C.M. Bertka, B.O. Mysen (Eds.), Mantle Petrology; Field Observations and High-Pressure Experimentation; a Tribute to Francis R. (Joe) Boyd, 1999.
[35] D.J. Frost, B.J. Wood, Experimental measurements of the fugacity of CO_2 and graphite/diamond stability from 35 to 77 kbar at 925 to 1650 degrees C, Geochim. Cosmochim. Acta 61 (1997) 1565–1574.
[36] D.J. Frost, B.J. Wood, The fugacity of carbon dioxide and the graphite/diamond CO equilibrium between 35 and 77 kbar at 925 to 1650 degrees C, Geochim. Cosmochim. Acta 62 (1998) 725–725.
[37] R. Brooker, J.R. Holloway, R. Hervig, Reduction in piston-cylinder experiments: the detection of carbon infiltration into platinum capsules, Am. Mineral. 83 (1998) 985–994.
[38] J. Ito, High temperature solvent growth of orthoenstatite, $MgSiO_3$ in air, Geophys. Res. Lett. 2 (1975) 533–536.
[39] M. Wiedenbeck, D. Rhede, R. Lieckefett, H. Witzki, Cryogenic SIMS and its applications in the earth sciences, Appl. Surf. Sci. 231-2 (2004) 888–892.
[40] E.J. Catlos, S.S. Sorensen, T.M. Harrison, Th–Pb ion-microprobe dating of allanite, Am. Mineral. 85 (2000) 633–648.
[41] A.A. Kadik, S.N. Shilobreeva, V.M. Minaev, V.I. Kovalenko, The carbon measurements in the upper mantle minerals by the $^{12}C(d,n)^{13}N$ nuclear reaction, Lunar Planet. Sci. 27 (1996) 631.
[42] R.G. Schwab, B. Freisleben, Fluid CO_2 inclusions in olivine and pyroxene and their behaviour under high pressure and temperature conditions, Bull. Mineral. 111 (1988) 297–306.
[43] R.J. Angel, A. Chopelas, N.L. Ross, Stability of high-density clinoenstatite at upper-mantle pressures, Nature 358 (1992) 322–324.
[44] F. Freund, Mechanism of the water and carbon dioxide solubility in oxides and silicates and the role of O^-, Contrib. Mineral. Petrol. 76 (1981) 474–482.
[45] W.S. Fyfe, Lattice energies, phase transformations and volatiles in the mantle, Phys. Earth Planet. Inter. 3 (1970) 196–200.
[46] T. Ernst, G. Mages, R.G. Schwab, Liquid CO_2 in olivine bombs; generated by decomposition of "orthocarbonates"? Fluid Incl. Res. 69 (1969) 16–17.
[47] T. Ernst, R.G. Schwab, A new theory on the formation and ascent of basic magmas with special respect to the undersaturated series, Proc. 24th Int. Geol.Congr., Montreal Section, vol. 14, 1972, pp. 28–33.
[48] R. Shannon, Revised effective ionic radii and systematic studies of interatomic distances in halides and chalcogenides, Acta Crystallogr. 32 (1976) 751–767.
[49] R.M. Hazen, Effects of temperature and pressure on crystal-structure of forsterite, Am. Mineral. 61 (1976) 1280–1293.
[50] Y. Kudoh, Y. Takeuchi, The crystal structure of forsterite Mg_2SiO_4 under high pressure up to 149 kb, Z. Kristallogr. 171 (1985) 291–302.
[51] J.R. Smyth, D.L. Bish, Crystal Structures and Cation Sites of the Rock-Forming Minerals, Boston, (1988). 332 pp.
[52] R.D. Shannon, C.T. Prewitt, Effective ionic radii in oxides and fluorides, Acta Crystallogr., B 25 (1968) 925–945.
[53] P. Deines, The carbon isotope geochemistry of mantle xenoliths, Earth Sci. Rev. 58 (2002) 247–278.
[54] P.J. Wyllie, W.L. Huang, J. Otto, A.P. Byrnes, Carbonation of peridotites and decarbonation of siliceous dolomites represented in the system CaO–MgO–SiO_2–CO_2 to 30 kbar, Tectonophysics 100 (1983) 359–388.
[55] D. Canil, Experimental study bearing on the absence of carbonate in mantle-derived xenoliths, Geology 18 (1990) 1011–1013.
[56] Y. Bottinga, M. Javoy, Mid-ocean ridge basalt degassing; bubble nucleation, J. Geophys. Res. 95 (1990) 5125–5131.
[57] T.M. Gerlach, K.A. McGee, T. Elias, A.J. Sutton, M.P. Doukas, Carbon dioxide emission rate of Kilauea Volcano: implications for primary magma and the summit reservoir, J. Geophys. Res. 107 (2002) 2189.
[58] T.M. Gerlach, E.J. Graeber, Volatile budget of Kilauea Volcano, Nature 313 (1985) 273–277.
[59] L.P. Greenland, W.I. Rose, J.B. Stokes, An estimate of gas emissions and magmatic gas content from Kilauea Volcano, Geochim. Cosmochim. Acta 49 (1985) 125–129.
[60] M. Javoy, F. Pineau, H. Delorme, Carbon and nitrogen isotopes in the mantle, Chem. Geol. 57 (1986) 41–62.
[61] Y. Zhang, A. Zindler, Distribution and evolution of carbon and nitrogen in Earth, Earth Planet. Sci. Lett. 117 (1993) 331–345.
[62] B. Marty, A. Jambon, $C/^3He$ in volatile fluxes from the solid Earth; implications for carbon geodynamics, Earth Planet. Sci. Lett. 83 (1987) 16–26.
[63] P.J. Wyllie, W.L. Huang, Carbonation and melting reactions in the system CaO–MgO–SiO_2–CO_2 at mantle pressures with geophysical and petrological applications, Contrib. Mineral. Petrol. 54 (1976) 79–107.
[64] J.A. Dalton, D.C. Presnall, Carbonatitic melts along the solidus of model lherzolite in the system CaO–MgO–Al_2O_3–SiO_2–CO_2 from 3 to 7 GPa, Contrib. Mineral. Petrol. 131 (1998) 123–135.
[65] D.P. Dobson, A.P. Jones, R. Rabe, T. Sekine, K. Kurita, T. Taniguchi, T. Kondo, T. Kato, O. Shimomura, S. Urakawa, In-situ measurements of viscosity and density of carbonate melts at high pressure, Earth Planet. Sci. Lett. 143 (1996) 207–215.
[66] M. Wilson, Igneous Petrogenesis, Unwin Hyman, London, 1989. 466 pp.
[67] J.C. McElwain, D.J. Beerling, F.I. Woodward, Fossil plants and global warming at the Triassic–Jurassic boundary, Science 285 (1999) 1386–1390.

[68] P. Wignall, The link between large igneous province eruptions and mass extinctions, Elements 1 (2005) 293–297.
[69] D. Bercovici, S. Karato, Whole-mantle convection and the transition-zone water filter, Nature 425 (2003) 39–44.
[70] B.J. Wood, L.T. Bryndzia, K.E. Johnson, Mantle oxidation state and its relationship to tectonic environment and fluid speciation, Science 245 (1990) 337–345.
[71] D. Canil, H.S.C. O'Neill, Distribution of ferric iron in some upper-mantle assemblages, J. Petrol. 37 (1996) 609–635.
[72] H.S.C. O'Neill, C.A. McCammon, D. Canil, D.C. Rubie, C.R. Ross, F. Seifert, Mossbauer spectroscopy of mantle transition zone phases and determination of minimum Fe^{3+} content, Am. Mineral. 78 (1993) 456–460.
[73] D.J. Frost, C. Liebske, F. Langenhorst, C.A. McCammon, R.G. Tronnes, D.C. Rubie, Experimental evidence for the existence of iron-rich metal in the Earth's lower mantle, Nature 428 (2004) 409–412.